Check for updates

Directing CO₂ electroreduction to ethanol *via* delicate geometrical modification of copper-based alloys†

Xiao Ma,‡[ab] Gong Zhang, [iD] ‡[ab] Jie Du,[ab] Xiaoyun Lin,[ab] Shiyu Zhen,[ab] Dongfang Cheng,[ab] Chaoxi Wang,[ab] Xin Chang, [iD] [ab] Shican Wu,[ab] Xiangcheng Shi,[abc] Lyudmila Moskaleva, [iD] [d] Peng Zhang, [iD] [abcefg] Zhi-Jian Zhao [iD] ⋆[abefg] and Jinlong Gong [iD] ⋆[abeh]

This paper describes a detailed simulation approach to simulate the redox process on CuZn alloys, bridging traditional calculations with large-scale, multi-step processes. Through comprehensive redox process simulation, we identify the specific active sites for ethanol production on redox-treated CuZn surfaces while establishing a universally applicable simulation method.

New concepts

This paper describes an innovative strategy to bridge traditional DFT calculations with large-scale and multi-step processes. By innovatively dividing the redox process into surface oxidation/reduction and oxygen diffusion processes, we reduced the complexity of the dynamics simulation process. Unlike previous work, which could only simulate single reaction processes, this innovative multi-equilibrium step simulation approach enables us to simulate the whole redox process on CuZn alloy catalysts, making it possible to trace the surface structure evolution of CuZn alloys during redox treatment and enabling us to gain detailed insight into special active sites for ethanol production. After the redox process, we classified the active sites by energy and geometric structure, indicating that the redox treatment creates several classes of specific active sites on CuZn surfaces. These sites alter the strength of the C–O bond in the selectivity-determining intermediate (*OC₂H₃), which is critical for ethanol formation. Specifically, Cu-rich step sites enhance ethanol selectivity by preserving the C–O bond. This work provides new insights into the mechanism of activity changes on oxide-derived CuZn surfaces through long-term simulation, which could potentially guide the precise design of electrocatalysts for renewable energy applications.

Introduction

The substantial emission of CO_2 has led to severe global climate change issues. CO_2 electroreduction (CO_2ER) utilizing copper-based catalysts has attracted significant attention due to its compatibility with renewable energy sources and its ability to produce multi-carbon products (C_{2+} products).[1–3] Among the various products, liquid ethanol emerges as a particularly promising candidate, exhibiting significant potential in energy storage owing to its facile storage characteristics, superior transportability, and high energy density.[4–9] However, monometallic Cu catalysts suffer from low coverage of *CO (the key C–C coupling intermediate on copper-based catalyst surfaces)[10–12] and high barriers of the rate-determining C–C coupling step,[13–18] which will hinder the formation of C_{2+} products, including ethanol (C_2H_5OH). Moreover, previous studies indicate that ethylene (C_2H_4), as the competing product, and ethanol share the same selectivity-determining intermediate (SDI) *OC₂H₃.[18,19] The cleavage *versus* preservation of the C–O bond in this SDI determines the selectivity.[19,20] Unfortunately, on the surface of monometallic Cu catalysts, the C–O bond in the SDI is relatively weak and easy to cleave,[19,21,22] leading to a relatively low faradaic efficiency ratio of ethanol to ethylene. Most of these ratios are lower than 1 for different types of Cu-based catalysts.[19,23–29]

Cu-based bimetallic systems have shown great potential to enhance ethanol yield. For instance, CO spillover effects over CuAg, CuAu and CuZn[30–33] alloys are believed to promote C_{2+} product formation by increasing local CO coverage. Additionally, Cu alloying with metals of different oxygen affinities directly impacts the C–

[a] School of Chemical Engineering & Technology, Key Laboratory for Green Chemical Technology of Ministry of Education, Tianjin University, Tianjin, 300072, China. E-mail: zjzhao@tju.edu.cn, jlgong@tju.edu.cn

[b] Collaborative Innovation Center for Chemical Science & Engineering (Tianjin), Tianjin, 300072, China

[c] Joint School of National University of Singapore and Tianjin University, International Campus of Tianjin University, Binhai New City, Fuzhou, 350207, Fujian, China

[d] Department of Chemistry, University of the Free State, P.O. Box 339, Bloemfontein 9301, South Africa

[e] International Joint Laboratory of Low-carbon Chemical Engineering, Tianjin 300350, China

[f] Haihe Laboratory of Sustainable Chemical Transformations, Tianjin 300192, China

[g] National Industry-Education Platform of Energy Storage, Tianjin University, 135 Yaguan Road, Tianjin 300350, China

[h] Tianjin Normal University, Tianjin 300387, China

† Electronic supplementary information (ESI) available. See DOI: https://doi.org/10.1039/d5mh00417a

‡ X. M. and G. Z. contributed equally.

O bond strength in SDI, thereby tuning the selectivity of C_{2+} products.[34] Among guest metals like Ag, Au, and Zn, CuZn catalysts are particularly attractive due to their cost-efficiency and ability to finely tune C–C coupling energies to enhance C_{2+} products (near to 0.67 eV).[35–37] Unfortunately, Zn atoms, with stronger oxygen affinity, may unfavorably affect C–O bond preservation and reduce ethanol production among C_{2+} products.[21,35] Additional methods are necessary to balance Zn atom oxygenophilicity to preserve the C–O bond.

Geometric structure regulation represents a promising approach for ethanol production, as demonstrated by recent studies identifying specific active sites on reconstructed Cu catalysts that selectively produce C_{2+} productions, especially ethanol production. The specific activity of the OD–Cu catalysts has attracted significant attention since the groundbreaking work by Kanan and colleagues.[38] For instance, Chorkendorff et al.[39] demonstrated through temperature-programmed desorption that redox-treated Cu catalysts exhibit multiple CO binding sites with distinct adsorption energies. Subsequently, isotope labeling studies by Ager et al.[40] established a direct correlation between these specific active sites and the formation of various C_{2+} products. These studies revealed that redox treatment of Cu surfaces could generate distinct active sites that promote the formation of C_{2+} products.

Further investigations have revealed that the enhanced C_{2+} selectivity can be attributed to specific low-coordination sites generated during this process. Goddard et al.[41,42] demonstrated that active sites on twin boundaries of Cu catalysts reduce the reaction energies of C–C coupling steps and promote C_{2+} production. Notably, detailed DFT calculations have elucidated that certain surface structures, particularly 4AD@Cu(100)[43] and step-square sites,[20] exhibit preferential activity toward ethanol production. The special sites for ethanol production on monometallic catalysts inspired us to investigate similar active sites on alloy systems by implementing redox processes on CuZn alloys.

CuZn-based catalysts have already demonstrated excellent catalytic properties for CO_2RR to ethanol. However, due to the unclear distribution and reconstruction of CuZn atoms, as well as the difficulty in characterizing specific surface structures on CuZn catalysts, researchers tend not to correlate ethanol production with active sites. Nevertheless, we hypothesize that there might be active sites similar to those on OD-Cu catalysts that promote ethanol production and that these sites may be one of the potential factors that have been overlooked.

Unfortunately, due to the similar atomic size of copper and zinc (Zn) and the insufficient spatial resolution of current in situ characterization techniques, detecting active sites for ethanol production on these catalysts remains challenging, hindering further development of CuZn catalysts. Although density functional theory (DFT) methods are widely employed for active site detection, quantum mechanics (QM) calculations are impractical for large-scale and long-term simulation on CuZn alloys. Moreover, the multistep and large-scale nature of the redox process complicates simulation of the reconstruction process on CuZn alloys, necessitating a strategy to simulate the dynamic reconstruction process on the catalyst.[20,42,44,45]

In this study, we employed a series of equilibrium steps to simulate the entire redox process, starting from the initial metallic CuZn alloy. The emergence of special active sites for ethanol during the redox process was verified. These sites demonstrate a collaborative effect between the geometric structure and the difference in the oxygen affinity of guest elements, altering the binding configuration of the selectivity-determining intermediate ($*OC_2H_3$) from a monodentate configuration to a bridge-like dual-bond configuration on Cu-rich step sites. This modification balances the negative effects caused by the oxygenophilicity of Zn atoms, strengthening the C–O bond and improving ethanol production. Based on these theoretical simulations and mechanistic insights, we employed a redox strategy to modify the surface configuration of CuZn alloys, achieving a high FE for ethanol under high current density ($>40\%$ at 300 mA cm^{-2}). This study demonstrates a theoretical framework for designing highly selective Cu-based catalysts through the synergistic control of alloy effects and geometric structures. Additionally, the developed simulation approach offers a universal framework for redox processes on metal surfaces. Furthermore, the integration of machine learning-accelerated theoretical calculations with experimental validation provides theoretical guidance for the rational design of the Cu-based alloys.

Results and discussion

Simulation protocols and active sites identification

Obtaining a realistic surface model is a prerequisite for exploring the redox-treated CuZn catalysts (i.e., OD-CuZn). To elucidate the precursor in the simulation process, we first conducted redox treatments on a series of CuZn alloys with different ratios. Experimentally, the catalyst with a Cu : Zn ratio close to 3 : 1 has the highest FE for C_{2+} products and ethanol (see details in Fig. S1, ESI†). Therefore, we used the metallic Cu_3Zn (111) surface as the initial state to start the molecular dynamics simulation with a neural network potential (NN-MD).[46,47] We divided the entire redox process into two main steps: oxidation under an oxygen atmosphere and the following reduction step under vacuum. The entire simulation workflow is shown in Fig. 1. To simulate the oxidation process of the CuZn alloy, we suggest that continuous oxidation contains two sequential sub steps: oxygen adsorption and diffusion. Considering that the oxidation process tends to occur at sites with higher oxygen binding energies,[48] we first calculated the adsorption energy of oxygen atoms (E_{*O}) on the initial CuZn surface using a neural network potential. We then sequentially added O atoms in order from highest to lowest E_{*O} and calculated the chemical potential of the adsorbed oxygen after each addition. When the chemical potential of oxygen approaches zero, the oxygen adsorption is terminated (see details in Fig. S2–S5, ESI†). Next, we simulated the diffusion using the canonical ensemble (NVT) by performing neural network molecular dynamics (NN-MD) simulations on surfaces covered by oxygen. Similar to previous studies on Cu oxidation,[49–52] we found that oxygen atoms prefer to adsorb around low coordinate sites and form oxides,
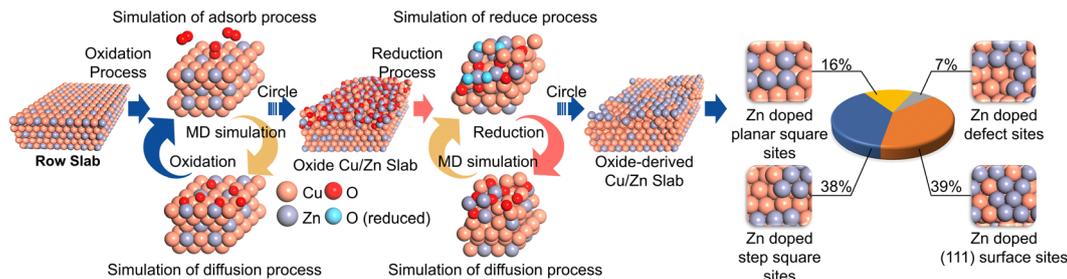
Fig. 1 Simulation of the redox process and the identification of different Zn doping modes. Simulation of the entire redox process, based on neural network accelerated chemical potential calculation and kinetic simulation. The temperature during simulation is set to room temperature. Surface geometry after redox process with diverse Zn doping modes, including Zn doped step-square sites, Zn doped (111) surface sites, Zn doped planar-square sites, and other Zn doped sites. These different sites might result in different product distribution.

then diffuse deeper through these oxides. By cycling between adsorption and diffusion processes, we successfully modelled the oxidation process of the CuZn alloy.

After obtaining a relatively stable CuZn alloy oxide, the simulation of the reduction process was initiated. This process, the reverse of oxidation, can be divided into sequential diffusion and removal sub-steps. First, canonical ensemble (NVT) kinetic simulations were employed to simulate oxygen migration and obtain a thermodynamically balanced structure. After the total energy of the system stabilizes, a relatively stable structure is obtained with oxygen accumulating near the surface. Subsequently, the oxygen removal process began.

In this process, we calculated the oxygen vacancy formation energy (E_{ov}) for each oxygen atom on the surface (see the Methods section in the ESI,† for the detailed formula), which considers the electrochemical reduction of oxygen to water. While this approach differs from conventional defect formation energy calculations[53] that typically yield positive values under thermodynamic equilibrium, our method specifically aims to identify the relative ease of oxygen reduction during the electrochemical process. We utilized the relative values of E_{ov} to determine the sequence for removing oxygen atoms to simulate the reduction process. This process created a partially reduced surface. This was followed by another round of NVT simulation to allow the system to reach equilibrium, during which subsurface oxygen atoms diffused to the surface. Following this protocol,[20,54,55] we developed a realistic surface model of OD-CuZn, in which oxygen atoms were either removed or trapped below the third layer, with the trapped oxygen shown to have minimal effect on the adsorption behaviors of adsorbates.[54,56]

For the OD-CuZn, obvious surface reconstruction is observed (see details in Fig. S6–S11, ESI†), generating a series of active sites with different Zn doping modes. To categorize these different sites, we used the binding energy of *CO and *OCCO intermediates (E_{*CO} and E_{*OCCO}) as descriptors to perform the high-throughput screening, given that they are key intermediates for C_{2+} products.[17,57] Combining the cluster analysis results of E_{*CO} and E_{*OCCO} with geometric structure information (see details in Fig. S12–S15, ESI†), we classified the existing surface sites into four groups (Fig. 1). Sites on (111) facets doped with Zn atoms accounted for the majority (39%), while step-square sites doped with Zn occupied a similar

percentage (38%). Lastly, planar-square and defect sites occupied relatively small proportions (16% and 7%, respectively). This suggests that the square sites (planar-square and step-square) are still the main sites for the generation of C_{2+} products. It seems that zinc doping does not affect the type of the main site for C_{2+} products.

Detailed DFT calculations of ethanol formation energy

To accurately explore the activity and selectivity of C_{2+} products and ethanol formation at these sites, we abstracted them into a series of slab models with different zinc doping modes for precise DFT calculations (see models and selection strategy in Fig. S12–S14, ESI†). Given that *CO dimerization represents the likely rate-limiting step in C_{2+} product formation (Fig. 2a), we employed the reaction energy of this elementary step as a descriptor to evaluate catalytic activity.

Our analysis encompassed 316 zinc-doped active sites, comprising 109 step-square sites, 107 planar-square sites, and 100 sites on (111) faces. To ensure unbiased sampling, these sites were randomly selected from both existing and optimized structures (detailed methodology provided in the ESI†). We found that for planar-square and step-square zinc-doped sites, their average *CO dimerization energies are significantly lower than those of Zn doped (111) surfaces and lower than those of pure copper sites with the same geometrical configurations (Fig. 2b). This finding is consistent with our cluster analysis results.

The reaction pathway toward ethanol and ethylene formation has been extensively investigated, with the *OC$_2$H$_3$ hydrogenation pathway being identified as thermodynamically favorable for C_2H_4/C_2H_5OH production. This pathway has gained considerable support from experimental observations and theoretical calculations, including studies on Cu(100) surfaces[19] and Cu vacancies,[22] and *OC$_2$H$_3$ has been widely recognized as a key intermediate in several influential works.[19,20,22,26,58] Although various intermediates have been proposed for CO_2 electroreduction to C_{2+} products,[59,60] *OC$_2$H$_3$ has emerged as a critical intermediate species owing to its favorable thermodynamic properties.[19] Our theoretical calculations further supported this understanding (Fig. S16, ESI†). Using *OC$_2$H$_3$ as the key intermediate, we investigated how the C–O bond activation varies across different surface sites. The pathway to ethylene proceeds through hydrogenation followed by C–O bond cleavage, whereas ethanol
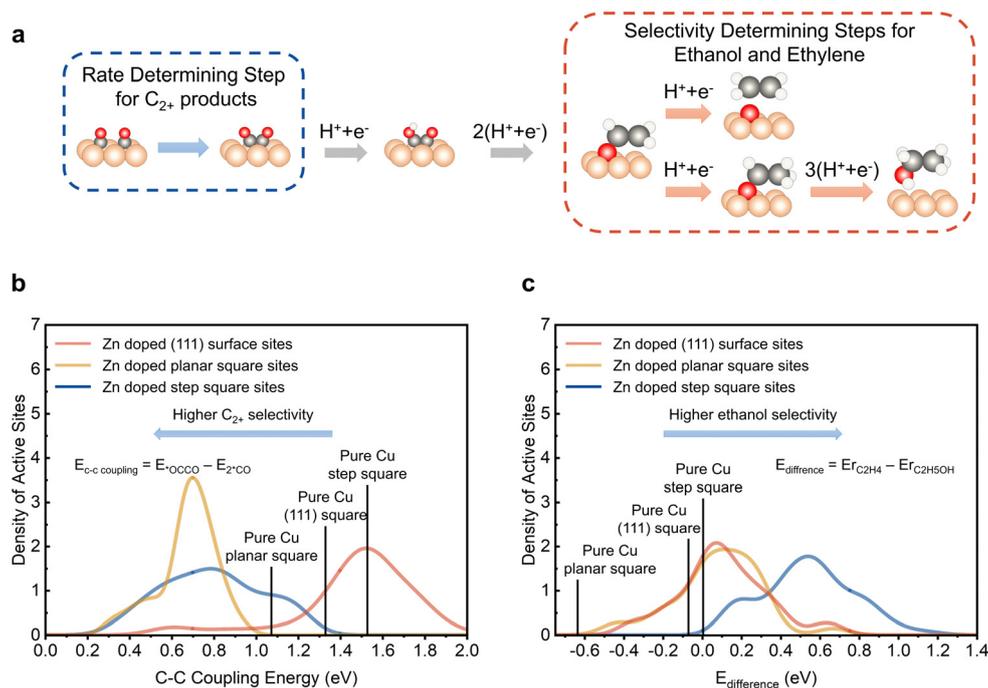
Fig. 2 The distribution of reaction energies on different active sites. (a) The possible reaction pathway of CO$_2$ER, including the C–C coupling step that determines C$_{2+}$ products (blue dotted frame) and the hydrogenation step of *OC$_2$H$_3$ that determines the selectivity of ethylene and ethanol (red dotted frame). Color code: brown-Cu; red-O; gray-C; white-H. (b) Reaction energy distribution of C–C coupling process, (c) hydrogenation process among three different Zn doping modes, the red sites are 111 sites, where blue and yellow active sites are step-square and planar-square sites.

formation occurs *via* direct protonation while maintaining the C–O bond. Using the difference between reaction energies of ethylene and ethanol ($Er_{C_2H_4}$ – $Er_{C_2H_5OH}$) as a descriptor, we constructed stacked histograms (Fig. 2c). We found that the step-square sites exhibited the largest energy difference compared to all other sites. Indicating that these sites could be the major source of high ethanol selectivity observed on the OD-CuZn surface.

To explain the molecular mechanism for high ethanol selectivity at these sites, we analyzed the C–O bond lengths of the *OC$_2$H$_3$ intermediate[20–22] on over 2000 active sites. We found that the C–O bond lengths primarily clustered into three major groups (Fig. 3a). The corresponding average bond lengths of these three groups are 1.36–1.38 Å, 1.31–1.33 Å, and 1.27–1.29 Å, respectively. Sites on doped (111) faces had the longest average bond length (1.36–1.38 Å), corresponding with the lowest ethanol selectivity, while the shorter bond lengths on zinc-doped planar-square (1.31–1.33 Å) likely corresponded to higher ethanol selectivity.

Interestingly, bond lengths on step-square sites were categorized into two subgroups: Cu-rich step sites (with more Cu atoms concentrated at the edge of the step) and Zn-rich step sites (with more Zn atoms concentrated at the edge of the step). Zn-rich step sites had an average C–O bond length of 1.31–1.33 Å, similar to that of zinc-doped planar-square sites, while Cu-rich step sites had an average length of 1.27–1.29 Å, shorter than other sites. This difference arises from the distinct adsorption configurations of the *OC$_2$H$_3$ intermediate (Fig. 3b). We found that on these sites, the adsorption configurations of the *OC$_2$H$_3$ intermediate differ, which might contribute to the difference in

bond length and energy. For Zn-rich step sites, the *OC$_2$H$_3$ intermediate tends to adsorb on the edge of the step sites in a monodentate configuration. In contrast, on Cu-rich step sites, it tends to adsorb on the terrace sites away from step sites in a bridge-like dual-bond configuration. To further explore the impact of adsorb configuration on selectivity, we calculated the free energy of the ethylene and ethanol formation (Fig. 3c and d). We found the difference of the free energy between ethylene and ethanol pathways is larger for the bridge-like dual-bond configuration, indicating a higher ethanol selectivity compared to the monodentate configuration. Moreover, we calculated the charge density difference and COHP in these adsorption configurations (Fig. S17, ESI†) and found that on the Zn-rich step sites, blue clouds appear on the C–O bond in the *OC$_2$H$_3$ intermediates, which indicates decreased charge density in the C–O bond, suggesting lower bond strength compared to the *OC$_2$H$_3$ intermediates on Cu-rich step sites. Additionally, the C–O bond antibonding orbitals on Cu-rich step sites show lower occupation below the Fermi level (E_F), indicating relatively stronger C–O bond strength at this site.

To gain a more detailed understanding of the kinetics, we additionally calculated the transition states to determine the C–O bond dissociation barriers.[61] The results were consistent with the thermodynamic trends (Fig. 3e), showing that the energy barrier on Cu-rich step sites is significantly higher than that on other sites. This suggests that these special active sites can stabilize the C–O bond in *OC$_2$H$_3$ intermediates by changing the adsorption configurations, which may increase ethanol selectivity.
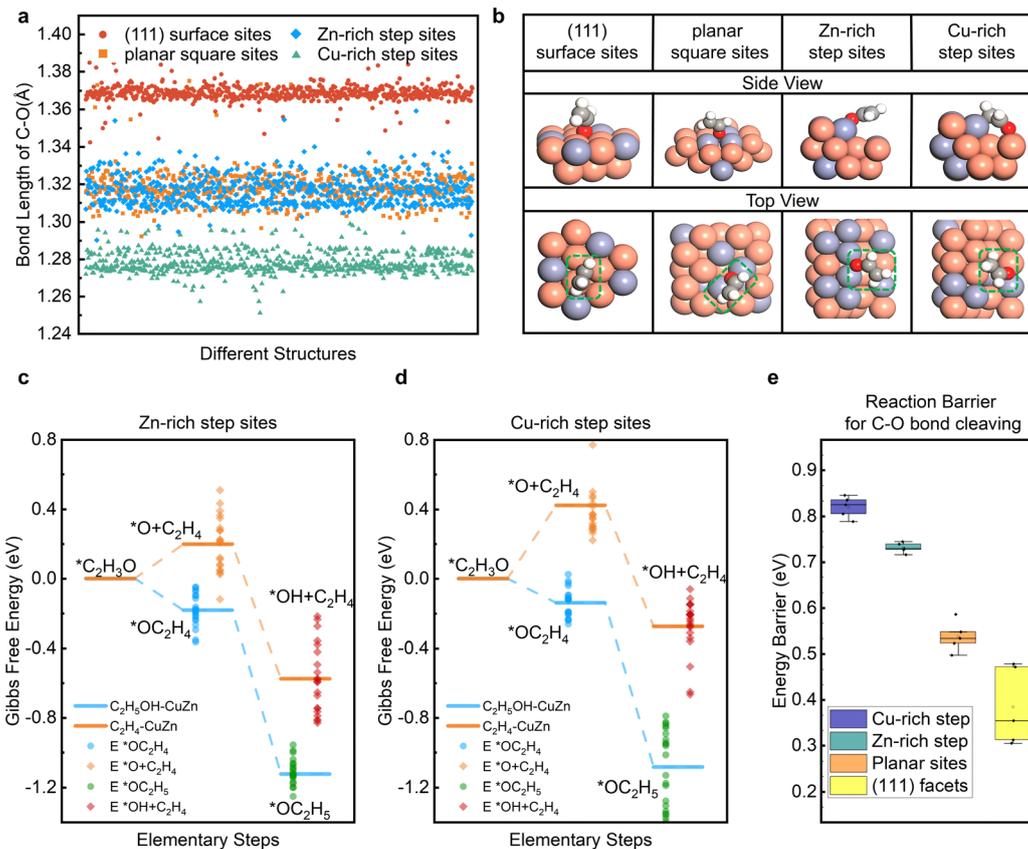
Fig. 3 Relationship of reaction free energy and reaction barrier with intermediate C−O lengths. (a) Statistical information on the C−O bond length of the SDI under different Zn doping modes. (b) Schematic diagrams of adsorption configurations for four different sites. (c) and (d) The reaction free energy of ethanol and ethylene. The horizontal line is the average of free energy of the two types of step square sites. The dots represent the free energy of each structure. (e) The reaction barriers for ethylene formation on different sites.

Experimental investigation of the effect of zinc doping modes on ethanol selectivity

Experimentally, we synthesized a series of OD-CuZn catalysts and sprayed them onto carbon paper (see details in Fig. S18, ESI†). The copper diffraction peaks in the X-ray diffraction (XRD) patterns are shifted with the increase of zinc ratio (see details in Fig. S19, ESI†), indicating that the catalyst remains in the alloy state without phase separation. The absence of zinc diffraction peaks suggests that the final OD-CuZn catalysts may contain low zinc doping concentration or highly dispersed zinc, which is consistent with the subsequent element mapping results (see details in Fig. S20, S21 and Table S2, ESI†). To investigate the surface composition, X-ray photoelectron spectroscopy (XPS) was employed to analyze the surface composition of the catalysts (Fig. S22 and S23, ESI†). All samples were transferred from the glove box to the XPS system using a vacuum transfer module (Thermo Scientific TM) to prevent surface oxidation during sample handling. The XPS results confirmed the complete absence of oxygen species on the surface of the oxide-derived CuZn (OD-CuZn) catalysts, corroborating our computational predictions of complete surface reduction under the experimental conditions.

We tested the CO_2 reduction performance of these samples. As expected, we observed higher partial current densities and FE for both C_{2+} products and ethanol compared to pure OD-Cu

catalysts (Fig. S24, ESI†). This indicates that there may be more effective active sites for ethanol production on the OD-CuZn catalyst than on the OD-Cu catalyst. These active sites likely correspond to the theoretically predicted configurations: Zn doped step square sites, Zn doped (111) facets, Zn doped planar square sites, and Zn doped defect sites. Subsequently we annealed these OD-CuZn samples. The annealing treatment reduced the number of sites available in the OD-CuZn catalysts and correspondingly reduced the number of sites we predicted, resulting in a decrease in the formation of the C_{2+} product from about 60% to about 30% and a decrease in the ethanol/ethylene ratio from 1.5 to 1.0.

To probe the surface site structures before and after annealing, we only focused on using CO as a probe molecule in *in situ* Raman spectroscopy. The CO vibrational features were monitored as they were highly sensitive to the local coordination environment of surface adsorption sites.[62–65] We observed that the CO peak on the untreated OD-CuZn was significantly broader than that on the annealed surface (Fig. 4a and b). Given that CO binding energies vary among different surface sites, the narrowing of the CO peak suggests a reduction in the diversity of surface sites after annealing. While C_{2+} intermediates were not detected here due to temporal resolution limits, future time-resolved spectroscopic studies may provide complementary insights, though this lies outside our
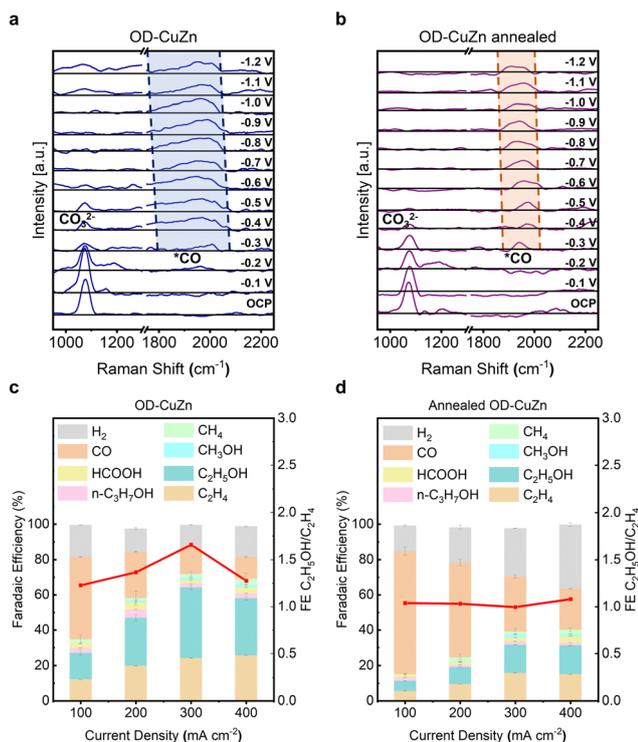
Fig. 4 Experimental exploration of zinc doping modes. (a) and (b) *In situ* Raman spectra of the OD-CuZn, a before and b after annealing. The *CO adsorption peak around 2000 cm^{-1} becomes significantly narrower after annealing. (c) and (d) Product distribution of OD-CuZn before a and b after annealing. It can be observed that the total C$_{2+}$ selectivity decreases markedly after annealing, while the selectivity of ethanol slightly declines. ((c) oxide-derived CuZn, (d) oxide-derived CuZn after annealing).

current focus on surface evolution. We also characterized the catalysts using transmission electron microscopy (TEM). After annealing, the lattice fringes showed a more uniform orientation (see details in Fig. S25 and S26, ESI†). This morphological evolution could lead to a decrease in the number of specific active sites. This observation is consistent with previous work demonstrating surface restructuring after thermal treatment,[20,39] and it aligns with the observed decrease in ethanol selectivity (Fig. 4c and d).

Conclusions

In conclusion, by combining theoretical calculations with experimental exploration, this work confirms that we can create highly active ethanol generation sites (Cu-rich step square sites) through redox treatment. These Cu-rich step square sites significantly increase the C–O bond strength of the selectivity-determining intermediate *OC$_2$H$_3$, thus greatly improving ethanol selectivity. This work highlights a strategy to tune the activity and selectivity of alloy catalysts by combining alloy effects with geometry effects, potentially contributing to the precise design of high-performance catalysts for industrial applications. Our discoveries provide novel insights into the synergistic effects of alloying and controllable reconstruction, indicating a pathway for generating catalysts with enhanced activities. This

work also lays the foundation for developing universal descriptors for C$_{2+}$ products on complex alloy surfaces.

In our future work, we intend to employ advanced characterization techniques, including *in situ* electrochemical cryo-electron microscopy or *in situ* electrochemical scanning tunnelling microscope with enhanced spatial resolution. These techniques will help overcome the current limitations in investigating site geometry, which will enable closer integration of experimental and theoretical calculations. Furthermore, we plan to establish more comprehensive scaling relationships to guide the rational design of catalysts. These efforts will advance our fundamental understanding of CO$_2$ electroreduction catalysis and accelerate the development of high-performance catalysts.

Computational methods

Neural-network-potential-based molecular dynamics

All neural-network-potential-based molecular dynamics (NN-MD) calculations were conducted using LASP,[47] a software widely used for large-scale simulations of complex chemical systems. The accuracy and part of the training data were shown in the ESI† (Fig. S27, S28 and Table S1, ESI†). Detailed information about the simulation of the CuZn alloy redox process is available in the ESI.†

DFT calculations

Density functional theory (DFT) calculations were carried out *via* Vienna Ab Initio Simulation software (VASP).[66,67] The electron exchange and correlation effects were described by the Perdew–Burke–Ernzerhof functional (PBE) form of the generalized gradient approximation (GGA).[68] In consideration of van der Waals correction for all systems, DFT-D3 method with Becke-Jonson damping was utilized.[69] The LOBSTER software[70] was used to process the COHP data. More details were described in the ESI.†

Experimental details

CO$_2$ reduction was conducted in a custom-designed three-chamber flow cell manufactured by Gaossunion Co., Ltd (details are provided in our previous work).[71] The redox processes were carried out at 675 K for 5 hours in a muffle furnace. Further details are described in the ESI.†

Author contributions

J. L. G. and Z. J. Z. supervised the project. J. L. G., Z.-J., Z., and X. M. conceptualized the project. X. M., G. Z., J. D. and P. Z. conducted the catalytic tests and the related data processing. X. M., X. Y. L., D. F. C., S. Y. Z. and X. C. carried out the theoretical calculations and simulation strategies. X. M., X. C. S. and S. C. W developed, tested and debugged programs. C. X. W. and J. D. provided *in situ* Raman results. All authors participated in writing the paper.

Data availability

The data that support the findings of this study are available from the corresponding author upon reasonable request. All codes are

available at our GitHub page: https://github.com/TJU-ECAT-AI/MD-simulation-for-redox-process. You can find all codes and surface structures on this page. The main codes for this program include Gen_structures.py, Makelogs.py, Read_energy.py, add_O2_first.py, clean_finder.py, main.py and validity.py. The.cif files in the directory OD-slabs are the structures simulated by this program.

Conflicts of interest

There are no conflicts to declare.

Acknowledgements

Notes and references

1 L. Xu, P. Trogadas and M.-O. Coppens, *Adv. Energy Mater.*, 2023, **13**, 2302974.

2 P. De Luna, C. Hahn, D. Higgins, S. A. Jaffer, T. F. Jaramillo and E. H. Sargent, *Science*, 2019, **364**, eaav3506.

3 T. O'Carroll, X. Yang, K. J. Gordon, L. Fei and G. Wu, *Adv. Energy Mater.*, 2024, 2401558.

4 F. Pan, X. Yang, T. O'Carroll, H. Li, K.-J. Chen and G. Wu, *Adv. Energy Mater.*, 2022, **12**, 2200586.

5 A. Vasileff, Y. Zhu, X. Zhi, Y. Zhao, L. Ge, H. M. Chen, Y. Zheng and S.-Z. Qiao, *Angew. Chem., Int. Ed.*, 2020, **59**, 19649–19653.

6 H. Shin, K. U. Hansen and F. Jiao, *Nat. Sustainable*, 2021, **4**, 911–919.

7 P. Tian, J. Su, Y. Song, R. Ye and M. Zhu, *Trans. Tianjin Univ.*, 2022, **28**, 73–79.

8 D. Gao, W. Li, H. Wang, G. Wang and R. Cai, *Trans. Tianjin Univ.*, 2022, **28**, 245–264.

9 H. Yao, M.-Y. Wang, C. Yue, B. Feng, W. Ji, C. Qian, S. Wang, S. Zhang and X. Ma, *Trans. Tianjin Univ.*, 2023, **29**, 254–274.

10 F. Pan, X. Duan, L. Fang, H. Li, Z. Xu, Y. Wang, T. Wang, T. Li, Z. Duan and K.-J. Chen, *Adv. Energy Mater.*, 2024, **14**, 2303118.

11 D. Bagchi, M. Riyaz, N. Dutta, G. Chawla, S. R. Churipard, A. Kumar Singh and S. C. Peter, *Adv. Energy Mater.*, 2024, 2402237.

12 S. Yan, Z. Chen, Y. Chen, C. Peng, X. Ma, X. Lv, Z. Qiu, Y. Yang, Y. Yang, M. Kuang, X. Xu and G. Zheng, *J. Am. Chem. Soc.*, 2023, **145**, 26374–26382.

13 K. J. P. Schouten, Z. Qin, E. Pérez Gallent and M. T. M. Koper, *J. Am. Chem. Soc.*, 2012, **134**, 9864–9867.

14 J. H. Montoya, A. A. Peterson and J. K. Nørskov, *Chem-CatChem*, 2013, **5**, 737–742.

15 J. H. Montoya, C. Shi, K. Chan and J. K. Nørskov, *J. Phys. Chem. Lett.*, 2015, **6**, 2032–2037.

16 E. Pérez-Gallent, M. C. Figueiredo, F. Calle-Vallejo and M. T. M. Koper, *Angew. Chem., Int. Ed.*, 2017, **56**, 3621–3624.

17 L. Wang, S. A. Nitopi, E. Bertheussen, M. Orazov, C. G. Morales-Guio, X. Liu, D. C. Higgins, K. Chan, J. K. Nørskov, C. Hahn and T. F. Jaramillo, *ACS Catal.*, 2018, **8**, 7445–7454.

18 Y. Zheng, A. Vasileff, X. Zhou, Y. Jiao, M. Jaroniec and S.-Z. Qiao, *J. Am. Chem. Soc.*, 2019, **141**, 7646–7659.

19 F. Calle-Vallejo and M. T. M. Koper, *Angew. Chem., Int. Ed.*, 2013, **52**, 7282–7285.

20 D. Cheng, Z.-J. Zhao, G. Zhang, P. Yang, L. Li, H. Gao, S. Liu, X. Chang, S. Chen, T. Wang, G. A. Ozin, Z. Liu and J. Gong, *Nat. Commun.*, 2021, **12**, 395.

21 Z. Li, P. Wang, X. Lyu, V. K. R. Kondapalli, S. Xiang, J. D. Jimenez, L. Ma, T. Ito, T. Zhang, J. Raj, Y. Fang, Y. Bai, J. Li, A. Serov, V. Shanov, A. I. Frenkel, S. D. Senanayake, S. Yang, T. P. Senftle and J. Wu, *Nat. Chem. Eng.*, 2024, **1**, 159–169.

22 T.-T. Zhuang, Z.-Q. Liang, A. Seifitokaldani, Y. Li, P. De Luna, T. Burdyny, F. Che, F. Meng, Y. Min, R. Quintero-Bermudez, C. T. Dinh, Y. Pang, M. Zhong, B. Zhang, J. Li, P.-N. Chen, X.-L. Zheng, H. Liang, W.-N. Ge, B.-J. Ye, D. Sinton, S.-H. Yu and E. H. Sargent, *Nat. Catal.*, 2018, **1**, 421–428.

23 Y. Hori, I. Takahashi, O. Koga and N. Hoshi, *J. Mol. Catal. A: Chem.*, 2003, **199**, 39–47.

24 Y. Kwon, Y. Lum, E. L. Clark, J. W. Ager and A. T. Bell, *ChemElectroChem*, 2016, **3**, 1012–1019.

25 A. Loiudice, P. Lobaccaro, E. A. Kamali, T. Thao, B. H. Huang, J. W. Ager and R. Buonsanti, *Angew. Chem., Int. Ed.*, 2016, **55**, 5789–5792.

26 S. Hanselman, M. T. M. Koper and F. Calle-Vallejo, *ACS Energy Lett.*, 2018, **3**, 1062–1067.

27 C. W. Li and M. W. Kanan, *J. Am. Chem. Soc.*, 2012, **134**, 7231–7234.

28 G. Jiang, D. Han, Z. Han, J. Gao, X. Wang, Z. Weng and Q.-H. Yang, *Trans. Tianjin Univ.*, 2022, **28**, 265–291.

29 Y. Ji, J. Du and A. Chen, *Trans. Tianjin Univ.*, 2022, **28**, 292–306.

30 J. Huang, M. Mensi, E. Oveisi, V. Mantella and R. Buonsanti, *J. Am. Chem. Soc.*, 2019, **141**, 2490–2499.

31 T. T. H. Hoang, S. Verma, S. Ma, T. T. Fister, J. Timoshenko, A. I. Frenkel, P. J. A. Kenis and A. A. Gewirth, *J. Am. Chem. Soc.*, 2018, **140**, 5791–5797.

32 D. Ren, B. S.-H. Ang and B. S. Yeo, *ACS Catal.*, 2016, **6**, 8239–8247.

33 S. Lee, G. Park and J. Lee, *ACS Catal.*, 2017, **7**, 8594–8604.

34 A. A. Peterson and J. K. Nørskov, *J. Phys. Chem. Lett.*, 2012, **3**, 251–258.

35 J. Du, G. Zhang, X. Ma, Q. Chang, H. Gao, C. Wang, X. Du, S. Li, T. Wang, Z.-J. Zhao, P. Zhang and J. Gong, *Adv. Funct. Mater.*, 2024, 2410339, DOI: 10.1002/adfm.202410339.

36 S. Zhen, G. Zhang, D. Cheng, H. Gao, L. Li, X. Lin, Z. Ding, Z. J. Zhao and J. Gong, *Angew. Chem., Int. Ed.*, 2022, **61**, e202201913.

37 M. Zhong, K. Tran, Y. Min, C. Wang, Z. Wang, C.-T. Dinh, P. De Luna, Z. Yu, A. S. Rasouli, P. Brodersen, S. Sun,

O. Voznyy, C.-S. Tan, M. Askerka, F. Che, M. Liu, A. Seifitokaldani, Y. Pang, S.-C. Lo, A. Ip, Z. Ulissi and E. H. Sargent, *Nature*, 2020, **581**, 178–183.

38 C. W. Li, J. Ciston and M. W. Kanan, *Nature*, 2014, **508**, 504–507.

39 A. Verdaguer-Casadevall, C. W. Li, T. P. Johansson, S. B. Scott, J. T. McKeown, M. Kumar, I. E. L. Stephens, M. W. Kanan and I. Chorkendorff, *J. Am. Chem. Soc.*, 2015, **137**, 9808–9811.

40 Y. Lum and J. W. Ager, *Nat. Catal.*, 2019, **2**, 86–93.

41 T. Cheng, H. Xiao and W. A. Goddard, *J. Am. Chem. Soc.*, 2017, **139**, 11642–11645.

42 Y. Huang, Y. Chen, T. Cheng, L.-W. Wang and W. A. Goddard, III, *ACS Energy Lett.*, 2018, **3**, 2983–2988.

43 O. Piqué, F. Viñes, F. Illas and F. Calle-Vallejo, *ACS Catal.*, 2020, **10**, 10488–10494.

44 Y. Chen, Y. Huang, T. Cheng and W. A. Goddard, III, *J. Am. Chem. Soc.*, 2019, **141**, 11651–11657.

45 D. Zhang, P. Yi, X. Lai, L. Peng and H. Li, *Nat. Commun.*, 2024, **15**, 344.

46 S.-D. Huang, C. Shang, X.-J. Zhang and Z.-P. Liu, *Chem. Sci.*, 2017, **8**, 6327–6337.

47 S. D. Huang, C. Shang, P. L. Kang, X. J. Zhang and Z. P. Liu, *WIREs Comput. Mol. Sci.*, 2019, 9.

48 Q. Zhu, Z. Pan, Z. Zhao, G. Cao, L. Luo, C. Ni, H. Wei, Z. Zhang, F. Sansoz and J. Wang, *Nat. Commun.*, 2021, **12**, 558.

49 L. Zou, J. Li, D. Zakharov, E. A. Stach and G. Zhou, *Nat. Commun.*, 2017, **8**, 307.

50 A. P. LaGrow, M. R. Ward, D. C. Lloyd, P. L. Gai and E. D. Boyes, *J. Am. Chem. Soc.*, 2017, **139**, 179–185.

51 S. Kunze, L. C. Tănase, M. J. Prieto, P. Grosse, F. Scholten, L. de Souza Caldas, D. van Vörden, T. Schmidt and B. R. Cuenya, *Chem. Sci.*, 2021, **12**, 14241–14253.

52 M. Li, M. T. Curnan, M. A. Gresh-Sill, S. D. House, W. A. Saidi and J. C. Yang, *Nat. Commun.*, 2021, **12**, 2781.

53 S. H. Wei and Y. Yan, in *Advanced Calculations for Defects in Materials*, ed. A. Alkauskas, P. Deák, J. Neugebauer, A. Pasquarello and C. G. Van De Walle, Wiley, 1 edn, 2011, pp. 213–239.

54 M. Fields, X. Hong, J. K. Nørskov and K. Chan, *J. Phys. Chem. C*, 2018, **122**, 16209–16215.

55 K. Li, X. Li, L. Li, X. Chang, S. Wu, C. Yang, X. Song, Z.-J. Zhao and J. Gong, *JACS Au*, 2023, **3**, 508–515.

56 A. Eilert, F. Cavalca, F. S. Roberts, J. Osterwalder, C. Liu, M. Favaro, E. J. Crumlin, H. Ogasawara, D. Friebel, L. G. M. Pettersson and A. Nilsson, *J. Phys. Chem. Lett.*, 2017, **8**, 285–290.

57 X. Liu, J. Xiao, H. Peng, X. Hong, K. Chan and J. K. Nørskov, *Nat. Commun.*, 2017, **8**, 15438.

58 M. Ma, K. Djanashvili and W. A. Smith, *Angew. Chem., Int. Ed.*, 2016, **55**, 6680–6684.

59 A. J. Garza, A. T. Bell and M. Head-Gordon, *ACS Catal.*, 2018, **8**, 1490–1499.

60 Y. Lum, T. Cheng, W. A. Goddard, III and J. W. Ager, *J. Am. Chem. Soc.*, 2018, **140**, 9337–9340.

61 C. Long, K. Wan, Y. Chen, L. Li, Y. Jiang, C. Yang, Q. Wu, G. Wu, P. Xu, J. Li, X. Shi, Z. Tang and C. Cui, *J. Am. Chem. Soc.*, 2024, **146**, 4632–4641.

62 Y. C. Li, Z. Wang, T. Yuan, D.-H. Nam, M. Luo, J. Wicks, B. Chen, J. Li, F. Li, F. P. G. de Arquer, Y. Wang, C.-T. Dinh, O. Voznyy, D. Sinton and E. H. Sargent, *J. Am. Chem. Soc.*, 2019, **141**, 8584–8591.

63 Y. Deng and B. S. Yeo, *ACS Catal.*, 2017, **7**, 7873–7889.

64 G. Blyholder, *J. Phys. Chem.*, 1964, **68**, 2772–2777.

65 H. Aizawa and S. Tsuneyuki, *Surf. Sci.*, 1998, **399**, L364–L370.

66 G. Kresse and J. Furthmüller, *Comput. Mater. Sci.*, 1996, **6**, 15–50.

67 G. Kresse and J. Hafner, *Phys. Rev. B: Condens. Matter Mater. Phys.*, 1994, **49**, 14251–14269.

68 J. P. Perdew, K. Burke and M. Ernzerhof, *Phys. Rev. Lett.*, 1997, **78**, 1396.

69 S. Grimme, S. Ehrlich and L. Goerigk, *J. Comput. Chem.*, 2011, 32.

70 S. Maintz, V. L. Deringer, A. L. Tchougréeff and R. Dronskowski, *J. Comput. Chem.*, 2016, **37**, 1030–1035.

71 G. Zhang, Z.-J. Zhao, D. Cheng, H. Li, J. Yu, Q. Wang, H. Gao, J. Guo, H. Wang, G. A. Ozin, T. Wang and J. Gong, *Nat. Commun.*, 2021, **12**, 5745.